PET/CT-Based Absorbed Dose Maps in ^{90}Y Selective Internal Radiation Therapy Correlate with Spatial Changes in Liver Function Derived from Dynamic MRI

Zhonglin Lu[1–3], Daniel F. Polan[4], Lise Wei[4], Madhava P. Aryal[4], Kellen Fitzpatrick[3], Chang Wang[5], Kyle C. Cuneo[4], Joseph R. Evans[4], Molly E. Roseland[3], Joseph J. Gemmete[3], Jared A. Christensen[3], Baljendra S. Kapoor[3], Justin K. Mikell[6], Yue Cao[3,4,7], Greta S.P. Mok[1,2,8], and Yuni K. Dewaraja[3]

[1]Biomedical Imaging Laboratory, Department of Electrical and Computer Engineering, Faculty of Science and Technology, University of Macau, Taipa, China; [2]Center for Cognitive and Brain Sciences, Institute of Collaborative Innovation, University of Macau, Taipa, China; [3]Department of Radiology, University of Michigan Medical Center, Ann Arbor, Michigan; [4]Department of Radiation Oncology, University of Michigan, Ann Arbor, Michigan; [5]Department of Biostatistics, University of Michigan, Ann Arbor, Michigan; [6]Department of Radiation Oncology, Washington University in St. Louis, St. Louis, Missouri; [7]Department of Biomedical Engineering, University of Michigan, Ann Arbor, Michigan; and [8]Ministry of Education Frontiers Science Center for Precision Oncology, Faculty of Health Science, University of Macau, Taipa, China

Functional liver parenchyma can be damaged from treatment of liver malignancies with ^{90}Y selective internal radiation therapy (SIRT). Evaluating functional parenchymal changes and developing an absorbed dose (AD)–toxicity model can assist the clinical management of patients receiving SIRT. We aimed to determine whether there is a correlation between ^{90}Y PET AD voxel maps and spatial changes in the nontumoral liver (NTL) function derived from dynamic gadoxetic acid–enhanced MRI before and after SIRT. **Methods:** Dynamic gadoxetic acid–enhanced MRI scans were acquired before and after treatment for 11 patients undergoing ^{90}Y SIRT. Gadoxetic acid uptake rate (k_1) maps that directly quantify spatial liver parenchymal function were generated from MRI data. Voxel-based AD maps, derived from the ^{90}Y PET/CT scans, were binned according to AD. Pre- and post-SIRT k_1 maps were coregistered to the AD map. Absolute and percentage k_1 loss in each bin was calculated as a measure of loss of liver function, and Spearman correlation coefficients between k_1 loss and AD were evaluated for each patient. Average k_1 loss over the patients was fit to a 3-parameter logistic function based on AD. Patients were further stratified into subgroups based on lesion type, baseline albumin–bilirubin scores and alanine transaminase levels, dose–volume effect, and number of SIRT treatments. **Results:** Significant positive correlations ($\rho = 0.53$–0.99, $P < 0.001$) between both absolute and percentage k_1 loss and AD were observed in most patients (8/11). The average k_1 loss over 9 patients also exhibited a significant strong correlation with AD ($\rho \geq 0.92$, $P < 0.001$). The average percentage k_1 loss of patients across AD bins was 28%, with a logistic function model demonstrating about a 25% k_1 loss at about 100 Gy. Analysis between patient subgroups demonstrated that k_1 loss was greater among patients with hepatocellular carcinoma, higher alanine transaminase levels, larger fractional volumes of NTL receiving an AD of 70 Gy or more, and sequential SIRT treatments. **Conclusion:** Novel application of multimodality imaging demonstrated a correlation between ^{90}Y SIRT AD and spatial functional liver parenchymal degradation, indicating that a higher AD is associated with a larger loss of local hepatocyte function. With the developed response models, PET-derived AD maps can potentially be used prospectively to identify localized damage in liver and to enhance treatment strategies.

Key Words: SIRT; ^{90}Y PET/CT; DGAE MRI; dosimetry; absorbed dose–toxicity relationship

Selective internal radiation therapy (SIRT) with ^{90}Y is an effective treatment for patients with unresectable primary or metastatic liver cancer. During SIRT, intraarterial administration of ^{90}Y microspheres leads to preferential deposition of microspheres and absorbed dose (AD) in and around tumors (*1*). However, on the basis of the surrounding arterial blood supply, some of the microspheres can deliver dose to nontumoral liver (NTL), resulting in radiation-associated toxicity to the NTL (*2*). Despite the potential for local heterogeneity, historically only mean AD within the NTL has been analyzed in correlation with the whole-liver toxicity biomarkers for dose–toxicity evaluation (*3–7*). As a tool for establishing a dose–toxicity relationship for the NTL, post-SIRT dosimetry based on ^{90}Y PET/CT could be valuable, given its ability to capture the AD heterogeneity at the voxel level (*1,8*). Analysis of voxel level dosimetry and association with spatial liver parenchymal function can enable refinement of treatment strategies and mitigation of potential radiation-associated toxicity. This includes identifying high-functioning liver parenchymal regions receiving low doses (*9*), which can be spared in subsequent single- and multimodality treatments.

Imaging techniques for quantifying regional liver function include dynamic ^{99m}Tc-iminodiacetic acid SPECT/CT (*10*) and dynamic contrast-enhanced MRI (*11–13*). MRI-based techniques that assess liver function are based on contrast uptake by hepatocytes and demonstrate distinct advantages over SPECT/CT, including higher image resolution and higher soft-tissue contrast. Portal venous perfusion maps from dynamic contrast-enhanced MRI have been used as a surrogate of liver function (*11*). More recently, techniques for estimating direct hepatic parenchymal uptake have been developed

using dynamic gadoxetic acid–enhanced (DGAE) MRI, which applies a hepatobiliary contrast agent that is specifically absorbed and excreted by functioning hepatocytes. With DGAE MRI, gadoxetic acid uptake rate (k_1) maps can be derived, which uniquely allow for direct assessment of spatial liver parenchymal function (12,13).

Prior studies have established a correlation between degradation of regional liver parenchymal function, assessed via DGAE MRI, and radiation dose from stereotactic body radiation therapy (SBRT) (14). However, the impact of AD on regional liver function in the context of ^{90}Y SIRT remains unclear. Combining post-SIRT voxel level dosimetry with spatial k_1 maps could assist in improving the current clinical understanding of radioembolization-induced hepatotoxicity. In this pioneering study, we aimed to use multimodality imaging to establish a correlation between the voxel-level AD in the NTL from ^{90}Y PET/CT and the spatial liver function deterioration, that is, k_1 loss from DGAE MRI before and after ^{90}Y SIRT.

MATERIALS AND METHODS

Patient Population

Eleven patients with hepatocellular carcinoma (HCC) or metastatic liver cancer received ^{90}Y SIRT along with pre- and posttreatment DGAE MRI scans from 2020 to 2023 as part of a prospective clinical trial (ClinicalTrials.gov identifier NCT04518748) (Supplemental Tables 1 and 2; supplemental materials are available at http://jnm.snmjournals.org). All patients signed an Institutional Review Board–approved informed consent form and met prespecified inclusion criteria (15). Ten patients received either a single-hepatic-lobe or segmental treatment or 2 sequential bilobar treatments with about a 1-mo interval. One patient underwent 2 sequential unilobar treatments with about a 1-mo interval to administer microspheres through multiple arterial blood supplies to a single lesion. ^{90}Y glass microspheres (TheraSphere; Boston Scientific) were prescribed for each treatment session following standard dosimetry practices at the discretion of the treating clinician (16). The administered activity ranged from 0.92 to 5.97 GBq (median, 3.28 GBq) per treatment. Liver parenchymal function and injury were assessed by various biomarkers before the ^{90}Y SIRT (Supplemental Table 1) and at 1, 3, and 6 mo after therapy. These included common liver enzymes (alanine transaminase [ALT] and aspartate aminotransferase [AST]) and validated clinical scoring systems with prognostic relevance among patients with liver disease, including the albumin–bilirubin (ALBI) score ([log10 bilirubin (μmol/L) $\times$ 0.66] + [albumin (g/L) $\times$ -0.085]) (17) and the Child–Pugh score.

DGAE MRI Acquisition and Processing

DGAE MR images of the liver were acquired about 1 wk before and about 1 mo after completion of SIRT. After a median of 18 min following intravenous injection of a single standard dose of gadoxetic acid (Eovist; Bayer Healthcare Pharmaceuticals Inc.), patients underwent the DGAE MRI scans on a 3-T scanner (Skyra; Siemens Healthineers). The DGAE MRI sequence was adapted from Simeth et al. (13), for example, an echo time/repetition time of 1.16/2.68 ms, a flip angle of 13.5°, a median temporal sampling rate of 8.8 s, a matrix size of 384 $\times$ 384 $\times$ 64, and a voxel size of 1.09 $\times$ 1.09 $\times$ 3.5–4.2 mm. Reference MRI volumes were selected for pre- and post-SIRT time-series DGAE MRI volumes. A rigid registration method, outlined by Johansson et al. (18), was used to register the DGAE MRI volumes to the reference volume for breathing motion correction, yielding acceptable results after review by the technologist for the current patient cohort. However, if the results were deemed unacceptable because of obvious misregistration for a patient, an in-house–developed deformable motion correction in k-space would be used as an alternative (19) in our general practice. Details of the k_1 map generation process have been reported previously (12,13). Briefly, the gadoxetic acid k_1, that is, k_1 maps (mL/100 g/min) quantifying liver function spatially, was derived by modeling DGAE MRI volumes through a single-input 2-compartment model. This process also facilitated the creation of blood distribution volume (v_{dis}) maps for reference in excluding main vessels in the NTL mask. Subsequently, k_1 and v_{dis} maps before and after SIRT were coregistered along with the rigid coregistration of corresponding reference MRI volumes (Fig. 1, step 1) using an in-house software (imFIAT) that has been rigorously evaluated in collaborative projects of the Quantitative Image Network of the National Cancer Institute (14).
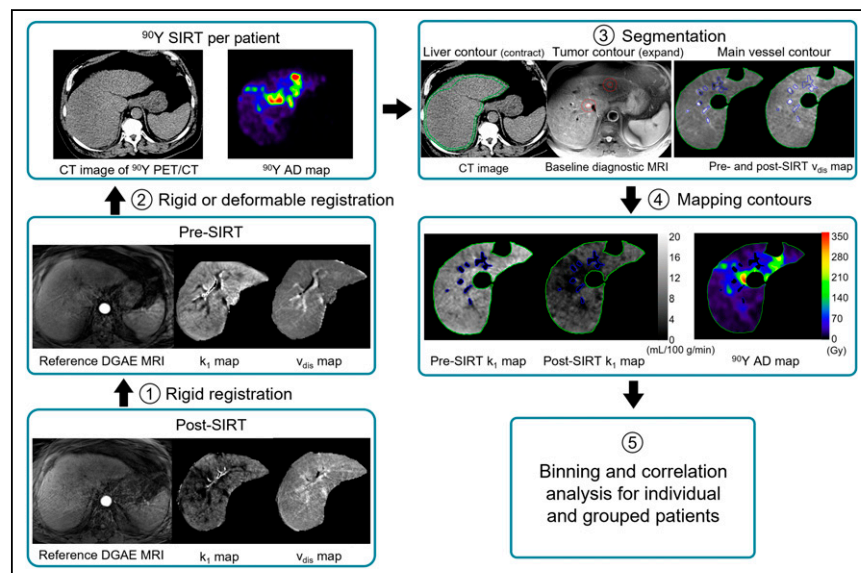
^{90}Y Microsphere PET/CT Imaging and Dosimetry

Details on post-SIRT ^{90}Y PET/CT imaging and dosimetry can be found in a previous publication (6). Briefly, within 4 h after SIRT, time-of-flight ^{90}Y PET/CT imaging was acquired on a Biograph mCT (Siemens Healthineers) for about 30 min and reconstructed using 3-dimensional ordered-subset expectation maximization (1 iteration, 21 subsets) and 5-mm gaussian postfiltering. The PET matrix size was 200 $\times$ 200 $\times$ 82–145 with a voxel size 4.07 $\times$ 4.07 $\times$ 3 mm. Voxel-based ^{90}Y AD maps were calculated directly from the quantitative ^{90}Y PET/CT (in Bq/cm^3) using the dose-planning method Monte Carlo code (20). For patients receiving sequential administrations, the CT image from the latter treatment was registered to the CT image from the first treatment, and the 2 corresponding aligned AD maps were summed to generate 1 AD map.

FIGURE 1. Flowchart illustrating correlation process between ^{90}Y AD and k_1 maps. Steps 1 and 2 involve aligning post-SIRT k_1, pre-SIRT k_1, and AD maps through coregistration of DGAE MRI and CT images. In step 3, liver is delineated on CT, excluding lesions and main vessels segmented on diagnostic MRI and v_{dis} maps. Step 4 entails mapping refined NTL regions onto both k_1 and AD maps for correlation analysis in step 5.

k_1 Maps and ^{90}Y AD Map Alignment and Processing

The liver contours were segmented on the pre-SIRT reference MRI and CT images

using deep learning–based segmentation tools (MIM Software Inc.) for registration guidance. Then, the reference MRI volumes were coregistered to the CT images using the surface-based rigid or regularized deformable registration in MIM software (Fig. 1, step 2). Subsequently, k_1 maps and v_{dis} maps were aligned to AD maps and linearly interpolated to match their size.

Lesions were contoured by an experienced radiologist on baseline MR images or contrast-enhanced CT images and transferred to the CT of the PET/CT. To mitigate edge artifacts in k_1 maps, spill-out effects, and blurring of lesions on NTL in AD maps, the NTL masks were created by contracting the liver contour by a 0.5-cm margin and excluding the lesion contours expanded by 1 cm (14). Additionally, as a k_1 map is valid for assessing the function of only nontumoral hepatocytes, main vessels were excluded from the NTL mask by excluding voxels with v_{dis} values of less than 0.02 or more than 0.25 for refinement (Fig. 1, step 3) (13). For patients with unilobar involvement in SIRT, the NTL mask was further split into treated and untreated lobes. The NTL area was then mapped out for AD and pre- and post-SIRT k_1 maps (Fig. 1, step 4).

Data Analysis

Dosimetry Metrics. Dose–volume histogram metrics, including mean AD and minimum AD to percentage NTL volume (from 30% to 90% with increments of 20%), were computed to provide additional insights into the AD distribution among patients. The percentage of the whole NTL volume receiving at least 70 Gy (denoted as $V_{70\ Gy}$ in %) were also evaluated, as 70 Gy has been suggested as the AD limit of NTL for SIRT (4).

Regional Liver Function–to–Dose Correlation Analysis. To analyze the regional function degradation after ^{90}Y SIRT for individual patients, the AD maps were binned in 5-Gy increments from 0 to 100 Gy, in 10-Gy increments from 100 to 150 Gy, and in 25-Gy increments for more than 150 Gy for noise reduction in higher-AD regions with a smaller number of voxels. Additionally, bins encompassing fewer than 100 voxels (equivalent to 0.19 cm^3), potentially more subjective to noise, were excluded from the study. k_1 maps of both pre-SIRT and post-SIRT were spatially binned on the basis of the AD binning, and the k_1 values were averaged over each bin. Both the absolute loss (Eq. 1) and percentage loss (Eq. 2) of mean k_1 values before and after SIRT were calculated. This strategy of binning first and then subtracting was confirmed to be more robust against noise and misregistration (14):

$$\Delta k_{1,i}(\text{mL}/100\ \text{g/min}) = k_{1,i}^{pre} - k_{1,i}^{post},\qquad \text{Eq. 1}$$

$$\Delta k_{1,i}(\%) = (k_{1,i}^{pre} - k_{1,i}^{post})/k_{1,i}^{pre} \times 100,\qquad \text{Eq. 2}$$

where $k_{1,i}^{pre}$ and $k_{1,i}^{post}$ stand for the mean k_1 in the i-th dose bin before and after SIRT, respectively. In patients with unilobar treatment only, the k_1 loss of the untreated lobe ($\sim$0 Gy) was calculated and compared with the first bin in the treated lobe, that is, low-AD (≤ 5 Gy) region. The linear regression model and Wilcoxon signed-rank testing were applied to assess numeric and statistical differences, respectively. If there was no obvious discrepancy in the values or a statistically significant difference ($P > 0.05$), the untreated lobe was combined with the treated lobe to incorporate more volume for greater correlation assessment.

The Spearman correlation analysis was used to evaluate the relationship between k_1 loss and AD for each patient.

For evaluation of the entire patient cohort, the absolute/percentage k_1 loss and AD were averaged over all patients for each bin, denoted as $\overline{\Delta k_{1,i}}$ and $\overline{AD_i}$, respectively. To develop a dose-function response model, a 3-parameter logistic function (Eq. 3) was fit, based on normal-tissue complication probability modeling:

$$\overline{\Delta k}_{1,i} = \frac{\alpha}{1 + e^{(D_c - \overline{AD_i})/\gamma}},\qquad \text{Eq. 3}$$

where α represents an asymptote indicating the maximum achievable k_1 loss, D_c denotes a characteristic dose at 50%-asymptotic height of the maximum loss, and γ is proportional to the inverse of the dose–response slope at D_c. This function was fit by applying a nonlinear least-squares function implemented in R (21). The goodness of fit was assessed using the coefficient of determination R^2 by the aomisc package in R (22) and the SE of fit variables. The k_1 loss averaged over all patients and all bins was computed for comparison. The patient cohort was further stratified into subgroups based on specific characteristics, including HCC or liver metastases, baseline ALBI scores, baseline ALT and AST levels, dose–volume effects ($V_{70\ Gy}$), and single versus sequential treatments. ALBI scores, ALT and AST levels, and $V_{70\ Gy}$ subgroups were defined using their respective median values as thresholds to ensure balanced subgroup sizes.

Global Liver Function Assessment Comparison. Global liver function measured through imaging (k_1 maps) and biomarkers (ALBI scores) was compared. Mean k_1 multiplied by NTL volume ($k_1 V_L$) as functional volume (13) were calculated before and after SIRT, and the difference represented global k_1 loss. Meanwhile, the change in ALBI scores after SIRT, corresponding to the time of the second DGAE MRI acquisition, was computed relative to the baseline. Pearson correlation analysis was performed between $k_1 V_L$ loss and the ALBI score increase.

RESULTS

Dosimetry Metrics

The dose–volume histogram plots and metrics in the entire NTL, including mean AD, D_{xx} (xx = 30%, 50%, 70%, and 90%), and $V_{70\ Gy}$ for 11 patients, are shown in Supplemental Figure 1 and Supplemental Table 2, respectively. The median value of the mean AD of the whole NTL was 35.1 Gy (range, 2.4–61.6 Gy), The median value of $V_{70\ Gy}$ was 7.8% (range, 0%–35.0%).

Regional Liver Function–to–AD Correlation Analysis

Individual Patient Assessment. The linear regression analysis between k_1 loss in the low-AD (≤ 5 Gy) region of the treated lobe versus the untreated lobe (Fig. 2) for 7 patients who received only unilobar treatment demonstrated an approximate line of equality (slope, 1.01; intercept, -3.83%). This trend suggested nearly identical k_1 loss between the low-AD region of the treated lobe and the untreated lobe. Additionally, no statistically significant difference was observed between the two ($P = 0.237$ for Wilcoxon
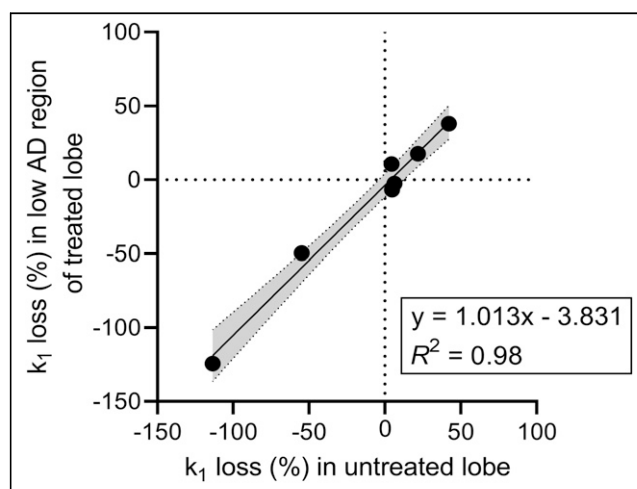

FIGURE 2. Scatterplot of k_1 loss in low-AD (≤ 5 Gy) region of treated lobe vs. untreated lobe. Best-fit line (solid line) combines with its 95% CI (gray area) as linear regression model.
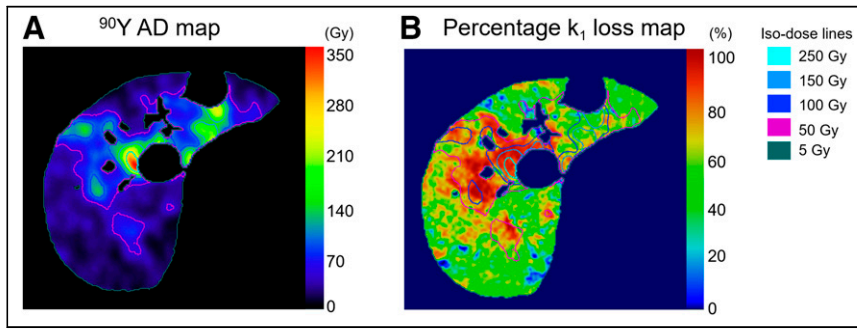
FIGURE 3. Sample visual correlation of ^{90}Y AD maps (A) and percentage k_1 loss (B) in refined NTL area, overlaid with isodose lines. Central hepatic region (segment 8) with higher AD presents larger k_1 loss. Percentage k_1 loss map is shown to visually illustrate its association with AD but was not directly used in correlation calculation analysis.

signed-rank test). Consequently, the untreated lobe was included in the correlation assessment between k_1 loss and AD.

Visual correlation between the percentage k_1 loss and AD maps in the refined NTL area, overlaid with isodose lines, is shown for a sample patient (patient 2) in Figure 3.

Scatterplots and Spearman correlation coefficients illustrate the relationship between k_1 loss and AD for 11 patients in Supplemental Figure 2 and Table 1, respectively. A significant and strong positive correlation ($\rho > 0.5$, $P < 0.001$) between both absolute and percentage k_1 loss and AD was observed in most patients (8/11), whereas 3 patients exhibited a poor or negative correlation. Most patients showed regional liver function degradation, particularly in higher-AD regions, except for 2 patients (patients 7 and 11) who demonstrated globally increased k_1 values after SIRT and were subsequently excluded from the grouped assessment because of this unexpected behavior.

Grouped Patient Assessment. Both absolute and percentage k_1 loss averaged over 9 patients exhibited a significantly strong positive correlation with the AD in the NTL (Fig. 4), with ρ values of at least 0.92 ($P < 0.001$) (Table 2). Logistic function modeling for k_1 loss and AD demonstrated an R^2 value of at least 0.91 for the percentage and absolute k_1 loss. The fit variables are given in Table 2. The average absolute and percentage k_1 loss over 9 patients across all AD bins was 2.2 mL/100 g/min and 28.1%, respectively.

Stratifying by patient characteristics, we found that most subgroups demonstrated a significantly strong correlation between AD and both absolute and percentage k_1 loss ($\rho > 0.9$, $P < 0.001$) (Supplemental Table 3), as well as a high R^2 for logistic model fitting (≥ 0.79), except subgroups with an ALBI of at least -2.93 and a lower $V_{70\ Gy}$. Because patients stratified by baseline ALT had results similar to those stratified by baseline AST, only the results of

ALT are presented here. The 3-parameter logistic model fit variables for subgroups are provided in Supplemental Table 3. Absolute (Supplemental Fig. 3) and percentage (Fig. 5) k_1 loss results displayed similar trends. When patients with HCC and liver metastases were compared, the HCC group exhibited a notably larger k_1 loss. Patients with a baseline ALT level of at least 45 IU/L had a more pronounced k_1 loss than did those with an ALT of less than 45 IU/L. In contrast, the subgroup with a baseline ALBI score of at least -2.93 presented a smaller k_1 loss than did the subgroup with an ALBI lower than -2.93. A lower $V_{70\ Gy}$ was associated with a generally smaller k_1 loss than was a higher $V_{70\ Gy}$. Additionally, patients with 2 sequential treatments demonstrated a larger k_1 loss than did patients with a single treatment.

Global Liver Function Assessment Comparison

Liver function changes after SIRT derived by imaging (k_1 maps) and biomarkers (change in ALBI score) showed a positive correlation ($r = 0.60$) for all 11 patients (Fig. 6), that is, a larger k_1V_L loss with increasing, less negative, ALBI scores (indicating rising bilirubin and lower albumin levels).

DISCUSSION

This study incorporated information from multimodality imaging (PET/CT and MRI) to establish a dose–toxicity relationship within normal liver after ^{90}Y SIRT; to our knowledge, this was the first attempt to assess this relationship at a spatial level. We demonstrated a strong and significant correlation between higher AD and an increasing k_1 loss for both individual ($\rho = 0.53$–0.99, $P < 0.001$ for 8/11) and grouped ($\rho \geq 0.92$, $P < 0.001$) patient studies. Additionally, in the grouped patient study, the average percentage k_1 loss across AD bins was 28.1%, with a logistic function model indicating that 25.8% of k_1 loss occurred at an AD of 102.1 Gy (Table 2).

The consistency for k_1 loss in the low-AD region of the treated lobe and untreated lobe suggests that at these low AD levels, k_1 loss is primarily the result of natural progression of liver malignancy. As AD levels increased, a corresponding increase in regional k_1 loss was observed, mirroring results from a prior study of patients undergoing SBRT (*14*). For patients exhibiting a poor or negative correlation, potential factors include the relatively dispersed and small perfused NTL volumes for patients 4 and 8 ($\sim$350 cm^3) and the narrow NTL AD ranges (0 to $\sim$25 Gy) for

TABLE 1
Spearman Correlation Coefficients Between Absolute and Percentage k_1 Loss and AD

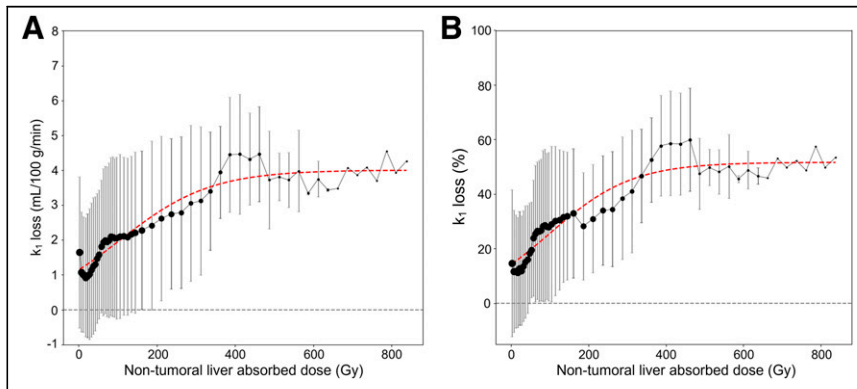| Loss	Patient no.										
	1	2	3	4	5	6	7	8	9	10	11
Absolute k_1	0.97*	0.53*	0.79*	−0.03	0.93*	0.72*	0.93*	0.09	−1.00*	0.67*	0.91*
Percentage k_1	0.98*	0.99*	0.89*	0.17	0.91*	0.76*	0.69*	0.18	−0.70	0.82*	0.89*

*$P < 0.001$.

FIGURE 4. Absolute loss (A) and percentage k_1 loss (B) vs. AD in NTL for 9 patients, with average and SD computed over all k_1 measurements. Red lines indicate fit 3-parameter logistic curves. Data point radius is proportional to patient count included in each bin.

patient 9, which may not provide enough sampling to establish a robust correlation. Generally, liver function degraded after therapy (i.e., lower k_1 values after SIRT for all except patients 7 and 11). This is an expected occurrence, inherent in SIRT, in the setting of radiation-induced liver injury. Interestingly, both patients who saw an unanticipated rise in k_1 values had received prior antivascular endothelial growth factor therapy with bevacizumab. It is possible this drug altered the vascular response or recovery after SIRT (which may alter enhancement and therefore k_1 values on DGAE MRI), although the small number of patients limits confident assessment. Nonetheless, the potential of such immunotherapy to generate spurious results warranted exclusion of these patients from our overall dose–response analysis.

For the grouped study, both curves in Figure 4 resemble a logistic function. Initially, there is a sharp rise in k_1 loss for an AD of less than 100 Gy, signifying pronounced functional decline. As AD increases, the rate of change in k_1 loss slows at about 200 Gy, indicating milder functional decline. However, fluctuations occur thereafter and are particularly notable after 400 Gy, which could be attributed to the reduced patient count within those bins. Specifically, large changes in slope at about 180 and 480 Gy may be attributed to patient dropout at higher-dose bins, marked by higher k_1 loss than in other patients. This possibility also may explain the slope change in Figures 5B and 5D at about 180 Gy.

Patient characteristics influenced the extent of k_1 loss in response to AD (Fig. 5). The HCC group exhibited a more pronounced k_1 loss, a more severe maximum liver function decline (α), and a lower AD to reach half this decline (D_c), than did the liver metastasis group, suggesting higher sensitivity to radiation in

HCC (23–25). One explanation for this finding is not the HCC itself but the higher incidence of cirrhosis among the HCC cohort (2/4 vs. 0/5 for HCC vs. liver metastases), which would limit the ability of background liver parenchyma to undergo repair and regeneration after radiation injury. Thus, we stratified patients into cirrhosis and noncirrhosis subgroups, with the cirrhosis subgroup showing a notably larger k_1 loss, albeit only 2 patients in our cohort had cirrhosis (Supplemental Fig. 4).

Child–Pugh scores and ascites were not used as stratification criteria because of limited variation (8/9 with A5 and no ascites). ALBI scores served as a surrogate for liver function over time and have been predictive of radiation-induced liver injury in HCC patients (17). Surprisingly, patients with initially normal ALBI scores showed higher k_1 loss, possibly because of having more functioning hepatocytes at baseline and, thus, a higher relative liver parenchymal loss resulting from any radiation-induced injury. However, the low median baseline ALBI score used as our cutoff (-2.93) and the limited number of cirrhosis and HCC patients in our study may make this score less reliable for predicting liver dysfunction in this subset. Conversely, higher baseline ALT and AST values were both associated with greater k_1 loss; because these markers indicate acute hepatocellular injury or cell death, it is unsurprising that subsequent radiation treatment would accentuate loss of liver function.

Regarding dose–volume effects, patients with a larger relative volume of the NTL receiving 70 Gy demonstrated generally larger k_1 loss and derived α. This implies a volume-based correlation between total irradiated volume and hepatic function damage, which is supported by prior studies (23,26). For assessment intervals, patients with sequential treatments had a longer (~3-mo) gap between pre- and post-SIRT MRI scans, whereas those with a single treatment had scans about 1 mo apart. Greater k_1 loss among the group with the sequential treatments also suggests that liver function could decline over time, compounding the effects of AD. However, the liver is known for its dynamic vascular reorganization and regeneration, which likely affects the comparison of these scans. Thus, a more detailed time interval stratification could be designed and assessed for a larger patient population in the future.

A comparison of the change in global liver function before and after SIRT estimated by k_1 maps and ALBI scores yielded a correlation of 0.60 (Fig. 6), consistent with the results of a previous

TABLE 2
Spearman Correlation Coefficients and 3-Parameter Logistic Model Fit Variables for Grouped 9 Patients

| Loss | ρ | Fit variable | | | |
		α	D_c (Gy)	γ (Gy)	R^2
Absolute k_1	0.93*	4.0 mL/100 g/min (0.1)	106.5 (10.1)	115.5 (13.2)	0.92
Percentage k_1	0.92*	51.6% (1.3)	102.1 (10.1)	105.6 (13.2)	0.91

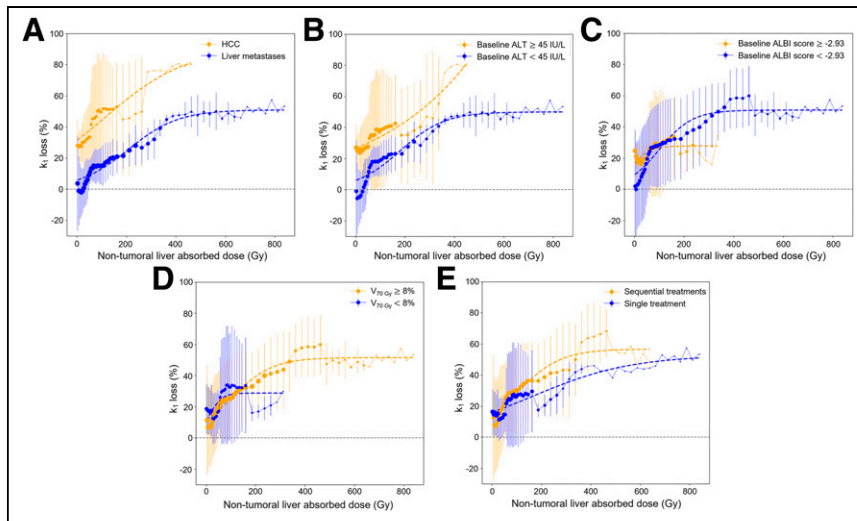*$P < 0.001$.
Data in parentheses are SE.

FIGURE 5. Percentage k_1 loss vs. AD in NTL for 9 patients subgrouped by HCC and liver metastases (A), baseline ALT $\geq$ and $<$ 45 IU/L (B), baseline ALBI score $\geq$ and $<$ −2.93 (C), $V_{70\,Gy}$ above and below median $V_{70\,Gy}$ (D), and single and sequential treatments (E). Dashed lines indicate fit 3-parameter logistic curves. Data point radius is proportional to patient count included in each bin.

study (*13*). Notably, the largest increase in ALBI score after SIRT was only 0.34, which may be reasonable considering most patients had good baseline liver function and all patients received a mean AD of less than 70 Gy. However, because of the heterogeneous distribution of AD and functional tissue in the NTL, radiation-induced liver damage may not be sufficiently captured by the ALBI biomarker. Furthermore, the regional dose–toxicity relationship for the NTL after SIRT in this study was more pronounced than in a prior study of whole-liver dose–toxicity relationships among patients with colorectal liver metastases by Alsultan et al. (*3*). They correlated the mean AD in the NTL from ^{90}Y PET/CT images with toxicity grades and changes in general liver biomarkers, such as total bilirubin, but a reliable association was not well established. In another study, by Chiesa et al. (*4*), the mean ADs in the NTL based on ^{99m}Tc-macroaggregated albumin SPECT/CT

images and basal bilirubin ($\geq$1.1 mg/dL) were reported as prognostic indicators for liver decompensation in patients with HCC. To explore this further, we stratified our patients into similar subgroups based on baseline bilirubin and found that patients with bilirubin of at least 1.1 mg/dL exhibited a larger percentage k_1 loss (Supplemental Fig. 5). However, with only 2 patients within this subgroup, only a limited assessment could be performed.

In an ongoing clinical trial (NCT04518748) of combinational therapy, the SBRT planning after SIRT is optimized to spare high-functioning regions of the liver based on pre-SBRT k_1 maps. The spatial level dose–toxicity correlations demonstrated in the current study could further facilitate refinement of SIRT dose selection and post-SIRT treatments, including SBRT. However, studies with larger patient cohorts are needed to establish the current findings. The small patient cohort limits statistical analysis and may compound errors in the analysis. Besides, there is a high variation in k_1 loss among individuals, as inferred from the large SD of k_1 loss when averaging over patients. Although a mixed model considering the dose as the fixed effect and patient as the random effect has been preliminarily explored, the limited number of patients rendered the modeling unrobust. An additional limitation associated with the small sample is that we chose to stratify subgroups on the basis of median values to ensure balanced groups, although a different approach (e.g., grade for ALBI) may be more relevant.

Another limitation is potential misregistration between single- and multimodality images due to involuntary and voluntary patient motion (*27*) and to hepatic volume changes (*28*), even with careful registration efforts. Our study used rigid registration between pre- and post-SIRT MRI scans, with results deemed acceptable after review by the technologist. However, further improvement may be achieved through nonrigid methods, which can better accommodate the deformable liver shape during patient motion, despite requiring careful deformation constraints and smoothness to avoid artifacts. To further alleviate the impact of misregistration, a binning strategy (*14*) was implemented by aggregating voxels with similar AD and spatial proximity into regions within a bin, which reduces susceptibility to misregistration compared with individual voxels. Motion correction strategies such as data-driven gating (*29*) were not used in this study because of lack of validation for ^{90}Y with low-count statistics. However, the impact of motion in ^{90}Y SIRT imaging may be less significant given the 5-mm image filter and the large untreated liver volumes in some patients. Moreover, a single snapshot of DGAE MRI was obtained after the completion of treatment, limiting this study to a short-term hepatic function assessment, whereas long-term dysfunction could be further explored.

Considering the technical aspect of this study, implementing DGAE MRI in clinical settings involves straightforward procedures for image acquisition and pharmacokinetic modeling. However, motion correction may present challenges and currently requires custom software, particularly if addressing respiratory motion in k-space. Additionally, advancements in newer generations of technology (*8*) offer superior sensitivity and event
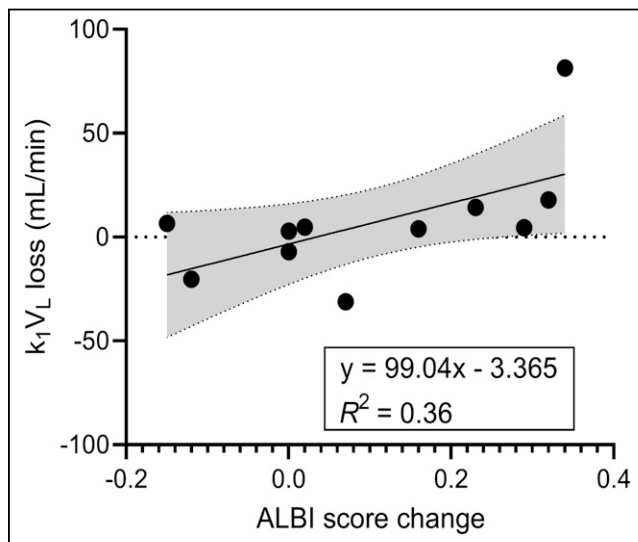

FIGURE 6. Scatterplot of global liver function changes after SIRT derived by k_1 maps vs. change in ALBI score. Best-fit line (solid line) combines with its 95% CI (gray area) as linear regression model.

statistics, particularly beneficial for ^{90}Y imaging. This facilitates achieving smaller voxel sizes while maintaining or enhancing signal-to-noise ratio. Consequently, we may be able to include the smaller dose-voxel bins (<100 voxels) that we currently exclude from our model. Furthermore, a smaller postprocessing filter kernel size may suffice, helping to maintain a higher spatial resolution in PET images and subsequent AD maps in the future.

CONCLUSION

In this pioneering study, information derived from multimodal imaging facilitated the correlation of regional liver function degradation, as quantified through DGAE MRI, with voxel-level AD in the NTL as determined by ^{90}Y PET/CT images after ^{90}Y SIRT. Higher AD levels are associated with a larger loss of liver function. Modeling demonstrates that patients with certain characteristics, such as HCC and a larger NTL fractional volume receiving an AD of 70 Gy or more and sequential SIRT treatments, could experience greater loss of liver function after treatment, warranting greater attention for their treatment. Future research with the inclusion of a larger and more diverse patient population is warranted to verify these findings.

DISCLOSURE

KEY POINTS

QUESTION: Is there a correlation between the ^{90}Y PET/CT-derived AD to the NTL and spatial liver function deterioration as assessed by dynamic MRI after ^{90}Y SIRT?

PERTINENT FINDINGS: A direct correlation between regions of higher ADs and increased liver function deterioration after SIRT has been demonstrated, with notably severer hepatic function loss in patients with HCC than in those with liver metastases.

IMPLICATIONS FOR PATIENT CARE: The nonuniform hepatic function loss is induced because of heterogeneous AD deposition. The spatial dose–toxicity information can potentially be used to enhance ^{90}Y SIRT strategies, including combination therapy.

REFERENCES

1. Chiesa C, Sjogreen-Gleisner K, Walrand S, et al. EANM dosimetry committee series on standard operational procedures: a unified methodology for ^{99m}Tc-MAA pre- and ^{90}Y peri-therapy dosimetry in liver radioembolization with ^{90}Y microspheres. *EJNMMI Phys.* 2021;8:77.

2. Sangro B, Gil-Alzugaray B, Rodriguez J, et al. Liver disease induced by radioembolization of liver tumors: description and possible risk factors. *Cancer.* 2008;112:1538–1546.

3. Alsultan AA, van Roekel C, Barentsz MW, et al. Dose–response and dose–toxicity relationships for glass ^{90}Y radioembolization in patients with liver metastases from colorectal cancer. *J Nucl Med.* 2021;62:1616–1623.

4. Chiesa C, Mira M, Bhoori S, et al. Radioembolization of hepatocarcinoma with ^{90}Y glass microspheres: treatment optimization using the dose-toxicity relationship. *Eur J Nucl Med Mol Imaging.* 2020;47:3018–3032.

5. Garin E, Lenoir L, Edeline J, et al. Boosted selective internal radiation therapy with ^{90}Y-loaded glass microspheres (B-SIRT) for hepatocellular carcinoma patients: a new personalized promising concept. *Eur J Nucl Med Mol Imaging.* 2013;40:1057–1068.

6. Dewaraja YK, Devasia T, Kaza RK, et al. Prediction of tumor control in ^{90}Y radioembolization by logit models with PET/CT-based dose metrics. *J Nucl Med.* 2020;61:104–111.

7. Strigari L, Sciuto R, Rea S, et al. Efficacy and toxicity related to treatment of hepatocellular carcinoma with ^{90}Y-SIR spheres: radiobiologic considerations. *J Nucl Med.* 2010;51:1377–1385.

8. Costa G, Spencer B, Omidvari N, et al. Radioembolization dosimetry with total-body ^{90}Y PET. *J Nucl Med.* 2022;63:1101–1107.

9. Matuszak MM, Kashani R, Green M, et al. Functional adaptation in radiation therapy. *Semin Radiat Oncol.* 2019;29:236–244.

10. Wang H, Cao Y. Spatially resolved assessment of hepatic function using ^{99m}Tc-IDA SPECT. *Med Phys.* 2013;40:092501.

11. Cao Y, Wang H, Johnson TD, et al. Prediction of liver function by using magnetic resonance-based portal venous perfusion imaging. *Int J Radiat Oncol Biol Phys.* 2013;85:258–263.

12. Simeth J, Johansson A, Owen D, et al. Quantification of liver function by linearization of a two-compartment model of gadoxetic acid uptake using dynamic contrast-enhanced magnetic resonance imaging. *NMR Biomed.* 2018;31:e3913.

13. Simeth J, Aryal M, Owen D, Cuneo K, Lawrence TS, Cao Y. Gadoxetic acid uptake rate as a measure of global and regional liver function as compared with indocyanine green retention, albumin-bilirubin score, and portal venous perfusion. *Adv Radiat Oncol.* 2022;7:100942.

14. Wei L, Simeth J, Aryal MP, et al. The effect of stereotactic body radiation therapy for hepatocellular cancer on regional hepatic liver function. *Int J Radiat Oncol Biol Phys.* 2023;115:794–802.

15. Combined Y-90 selective internal radiation therapy (Y-90 SIRT) and stereotactic body radiation therapy (SBRT) in hepatic malignancy. ClinicalTrials.gov website. https://clinicaltrials.gov/ct2/show/NCT04518748. Updated October 16, 2023. Accessed May 15, 2024.

16. Instructions for use: TheraSphere^{TM} ytrium-90 glass microspheres. Boston Scientific website. https://www.bostonscientific.com/content/dam/elabeling/pi/OTT-00221_Rev1_TheraSphere_en_s.pdf. Revised March 2021. Accessed May 15, 2024.

17. Lescure C, Estrade F, Pedrono M, et al. ALBI score is a strong predictor of toxicity following SIRT for hepatocellular carcinoma. *Cancers (Basel).* 2021;13:3794.

18. Johansson A, Balter J, Feng M, Cao Y. An overdetermined system of transform equations in support of robust DCE-MRI registration with outlier rejection. *Tomography.* 2016;2:188–196.

19. Johansson A, Balter JM, Cao Y. Abdominal DCE-MRI reconstruction with deformable motion correction for liver perfusion quantification. *Med Phys.* 2018;45:4529–4540.

20. Wilderman SJ, Dewaraja Y. Method for fast CT/SPECT-based 3D Monte Carlo absorbed dose computations in internal emitter therapy. *IEEE Trans Nucl Sci.* 2007;54:146–151.

21. bbmle: tools for general maximum likelihood estimation. The Comprehensive R Archive Network website. https://cran.r-project.org/web/packages/bbmle/index.html. Published December 9, 2023. Accessed May 15, 2024.

22. Schabenberger O, Pierce FJ. *Contemporary Statistical Models for the Plant and Soil Sciences*: CRC Press; 2001:251–261.

23. Dawson LA, Normolle D, Balter JM, McGinn CJ, Lawrence TS, Ten Haken RK. Analysis of radiation-induced liver disease using the Lyman NTCP model. *Int J Radiat Oncol Biol Phys.* 2002;53:810–821.

24. Xu Z-Y, Liang S-X, Zhu J, et al. Prediction of radiation-induced liver disease by Lyman normal-tissue complication probability model in three-dimensional conformal radiation therapy for primary liver carcinoma. *Int J Radiat Oncol Biol Phys.* 2006;65:189–195.

25. Miften M, Vinogradskiy Y, Moiseenko V, et al. Radiation dose-volume effects for liver SBRT. *Int J Radiat Oncol Biol Phys.* 2021;110:196–205.

26. Pan CC, Kavanagh BD, Dawson LA, et al. Radiation-associated liver injury. *Int J Radiat Oncol Biol Phys.* 2010;76(suppl):S94–S100.

27. Lu Z, Chen G, Jiang H, Sun J, Lin K-H, Mok GS. SPECT and CT misregistration reduction in [^{99m}Tc]Tc-MAA SPECT/CT for precision liver radioembolization treatment planning. *Eur J Nucl Med Mol Imaging.* 2023;50:2319–2330.

28. Polan DF, Feng M, Lawrence TS, Ten Haken RK, Brock KK. Implementing radiation dose-volume liver response in biomechanical deformable image registration. *Int J Radiat Oncol Biol Phys.* 2017;99:1004–1012.

29. Dias AH, Schleyer P, Vendelbo MH, Hjorthaug K, Gormsen LC, Munk OL. Clinical feasibility and impact of data-driven respiratory motion compensation studied in 200 whole-body ^{18}F-FDG PET/CT scans. *EJNMMI Res.* 2022;12:16.